Check for updates

Advanced Theory and Simulations

ADVANCED THEORY AND SIMULATIONS
www.advtheorysimul.com

RESEARCH ARTICLE OPEN ACCESS

Exploring X_2BH_6 (X = Li, Na, and K) Double Perovskite Hydrides for Solid-State Hydrogen Storage Applications

Aysenur Gencer[1] | Ahmet Aydogan[2] | Ozge Surucu[3,4] | Gokhan Surucu[5]

[1]Department of Physics, K. O. Faculty of Science, Karamanoglu Mehmetbey University, Karaman, Türkiye | [2]Graduate School of Natural and Applied Sciences, Karamanoglu Mehmetbey University, Karaman, Türkiye | [3]Department of Energy Systems Engineering, Faculty of Engineering and Natural Sciences, Ankara Yildirim Beyazit University, Ankara, Türkiye | [4]The Center for Third Generation Solar Cells Research and Applications (SOLAR 3.0), Ankara Yıldırım Beyazıt University, Ankara, Türkiye | [5]Department of Energy Systems Engineering, Faculty of Technology, Gazi University, Ankara, Türkiye

Correspondence: Aysenur Gencer (agencer@kmu.edu.tr)

Received: 24 April 2026 | **Revised:** 28 July 2026 | **Accepted:** 18 August 2026

Keywords: density functional theory | double perovskite hydrides | electronic properties | hydrogen storage | mechanical properties | phonon stability

ABSTRACT

Solid-state hydrogen storage in lightweight hydrides represents a promising pathway toward a sustainable hydrogen economy. In this work, we employ density functional theory to systematically investigate the structural, electronic, mechanical, dynamical, and hydrogen storage properties of X_2BH_6 (X = Li, Na, and K) hydrides. All hydrides exhibit negative formation energies, confirming their thermodynamic stability. The gravimetric hydrogen storage capacities are remarkably high: 19.71, 9.64, and 6.37 wt% for Li_2BH_6, Na_2BH_6, and K_2BH_6, respectively, all surpassing the 2025 U.S. Department of Energy target of 5.5 wt%. Electronic band structure analysis reveals metallic character for all hydrides. Evaluation of Born mechanical stability criteria reveals that Li_2BH_6 and K_2BH_6 are mechanically stable, whereas Na_2BH_6 is mechanically unstable. Phonon dispersion calculations demonstrate that only K_2BH_6 is dynamically stable, while Li_2BH_6 and Na_2BH_6 exhibit imaginary phonon modes. Combining all stability criteria, K_2BH_6 emerges as the most promising candidate, possessing simultaneous thermodynamic, mechanical, and dynamical stability alongside a gravimetric capacity of 6.37 wt% and a hydrogen desorption temperature of 308.00 K that falls within the DOE operating target. These findings suggest K_2BH_6 as a potential candidate for solid-state hydrogen storage and provide theoretical guidance for future experimental synthesis.

1 | Introduction

The escalating global energy demand, driven by rapid technological development and population growth, necessitates an urgent transition from fossil fuels to sustainable and clean energy carriers [1–3]. Hydrogen has attracted considerable attention as a next-generation energy carrier owing to its high gravimetric energy density (approximately 120 MJ/kg, roughly three times that of gasoline), its abundance, and the environmentally benign nature of its combustion, which yields only water as a by-product [4–7]. However, the realization of a viable hydrogen economy hinges upon overcoming key technological challenges in hydrogen production, storage, safety, and end-use applications [8, 9].

Among these challenges, efficient and safe hydrogen storage remains a critical bottleneck [10–12]. Current storage approaches are broadly classified into three categories: compressed gas, cryogenic liquid, and solid-state storage [13–15]. Compressed gas storage, while technologically mature, requires high-pressure vessels (350–700 bar) with inherent safety concerns and limited volumetric capacity [16–19]. Cryogenic liquid storage demands substantial energy input for cooling hydrogen to 20 K and is further limited by boil-off losses during extended storage periods

This is an open access article under the terms of the Creative Commons Attribution-NonCommercial-NoDerivs License, which permits use and distribution in any medium, provided the original work is properly cited, the use is non-commercial and no modifications or adaptations are made.
© 2026 The Author(s). *Advanced Theory and Simulations* published by Wiley-VCH GmbH

[20–23]. In contrast, solid-state hydrogen storage has emerged as a particularly promising alternative, offering inherent safety advantages and potentially superior volumetric energy densities [24].

Solid state storage mechanisms are classified into physisorption, in which molecular hydrogen adsorbs onto materials with high surface areas such as carbon nanostructures and metal organic frameworks [25, 26]. They also include chemisorption, where atomic hydrogen forms chemical bonds with host materials, as exemplified by metal hydrides and complex hydrides [27–31]. Among chemisorption-based materials, perovskite-type and double perovskite hydrides have garnered significant research interest in recent years due to their structural versatility and tunable hydrogen storage properties [32–41]. Several recent studies have explored double perovskite hydrides for hydrogen storage applications. Ahmed et al. [42] reported a gravimetric hydrogen storage capacity of 4.28 wt% for Ca_2FeH_6 in their investigation of X_2FeH_6 (X = Ca, Sr) double perovskites. Almahmoud et al. [43] systematically studied Y_2CoH_6 (Y = Ca, Ba, Mg, Sr) and demonstrated that all studied hydrides are mechanically and thermodynamically stable, with Mg_2CoH_6 exhibiting the highest gravimetric capacity of 5.32 wt%. Candan et al. [34] revealed that A_2SiH_6 (A = Li, Na) double perovskites show considerable potential for hydrogen storage, while Alkhaldi [32] investigated X_2VH_6 (X = Li, Na, K) and reported storage capacities meeting DOE targets. These studies collectively underscore the potential of lightweight double perovskite hydrides as promising hydrogen storage media.

In this study, we employ density functional theory (DFT) calculations to comprehensively investigate the structural, electronic, mechanical, dynamical, and hydrogen storage properties of X_2BH_6 (X = Li, Na, and K) double perovskite hydrides. The choice of these compositions is based on the use of boron, which is the lightest element in Group 13. Combined with light alkali metals, it is anticipated to provide the maximum gravimetric hydrogen storage capacity. To the best of our knowledge, these specific double perovskite hydride compositions have not been previously investigated. Our objective is to provide a thorough theoretical assessment of their viability for solid-state hydrogen storage by evaluating them against the targets established by the U.S. Department of Energy (DOE).

2 | Computational Details

First-principles calculations based on density functional theory (DFT) were performed using the Vienna Ab Initio Simulation Package (VASP) [44, 45]. The exchange–correlation interactions were treated within the generalized gradient approximation (GGA) using the Perdew–Burke–Ernzerhof (PBE) functional [46], and the electron–ion interactions were described by the projector augmented wave (PAW) method [47, 48]. The kinetic energy cutoff for the plane-wave basis set was set to 424 eV, and Brillouin zone sampling was performed using a Γ-centered scheme [49] with a 8×8×8 **k**-point grid. The valence electron configurations employed in the PAW potentials were: Li ($2s^1$), Na ($3s^1$), K ($4s^1$), B ($2s^22p^1$), and H ($1s^1$).

Structural optimizations were carried out until the total energy converged to within 10^{-9} eV per unit cell and the Hellmann–Feynman forces on each atom fell below 10^{-8} eV/Å. Bader charge analysis was performed using the algorithm developed by Henkelman et al. [50], based on the quantum theory of atoms in molecules formalism [51]. Electronic band structures were computed along the high-symmetry paths of the first Brillouin zone for the face-centered cubic lattice and visualized using the SUMO package [52].

The elastic stiffness tensor was determined via the stress–strain method implemented in VASP [53] from which the independent elastic constants for the cubic crystal system (C_{11}, C_{12}, and C_{44}) were extracted. The polycrystalline bulk modulus (B), shear modulus (G), and Young's modulus (E) were obtained using the Voigt–Reuss–Hill (VRH) averaging scheme [54]. Lattice dynamical properties were investigated using the finite displacement method as implemented in the PHONOPY code [55, 56], employing 2×2×2 supercells. X-ray diffraction patterns were simulated using the VESTA visualization software [57] with Cu Kα radiation (λ = 1.5418 Å). Moreover, the Ab-Initio molecular dynamics calculations were carried out at standard pressure and 300 K temperature. The positions of the atoms and the size of the unit cells were used as the variables. The desired results were achieved by utilizing the Langevin thermostat [58, 59] with 3, 7, 7, 3, 3, and 6 ps^{-1} atomic frictions for the Li, Na, K, B, and H atoms and lattice frictions, respectively. The equations of motion related to the ions were integrated using the Verlet algorithm with an integration time step of 1 fs. As is well documented, the computation of AIMD calculations is expensive and time-consuming. This promotes the integration of machine-learned force fields within VASP [60, 61]. A robust and effective framework for description and analysis is offered by descriptors based on the Gaussian representation of atomic distributions [61, 62] in the context of machine-learned potential energy surfaces. Furthermore, the target properties, which include energy, forces and stress tensor components, were obtained using Bayesian linear regression [60, 63], a method that provides accurate results.

3 | Results and Discussions

3.1 | Structural and Hydrogen Storage Properties

The investigated X_2BH_6 (X denoting Li, Na or K) system belongs to an emergent and highly promising category of functional materials termed vacancy-ordered double perovskite hydrides (A_2BH_6, or VODPH) [64, 65]. In contradistinction to conventional double perovskites ($A_2BB'H_6$), the VODPH architecture is distinguished by the complete and orderly omission of the secondary (B') cation site. This results in a structurally stable framework that is represented as $A_2B\Delta H$, where the Δ denotes a structural vacancy [64, 65]. The present vacancy-ordered arrangement is unique in its introduction of a high degree of structural flexibility, in addition to the provision of expansive interstitial pathways, which are of considerable benefit to hydrogen mobility and storage [64, 65]. Recently, there has been a surge of interest in sister VODPH systems, including Li_2SiH_6 and Na_2SiH_6, owing to their advantageous lightweight properties [34]. This work makes a direct contribution to the systematic understanding of structure-property relationships in vacancy-driven complex hydrides. The studied X_2BH_6 series is framed within the VODPH paradigm.

25130390, 2026, 9, Downloaded from https://advanced.onlinelibrary.wiley.com/doi/10.1002/adts.70534 by Turkey Cochrane Evidence Aid, Wiley Online Library on [31/08/2026]. See the Terms and Conditions (https://onlinelibrary.wiley.com/terms-and-conditions) on Wiley Online Library for rules of use; OA articles are governed by the applicable Creative Commons License

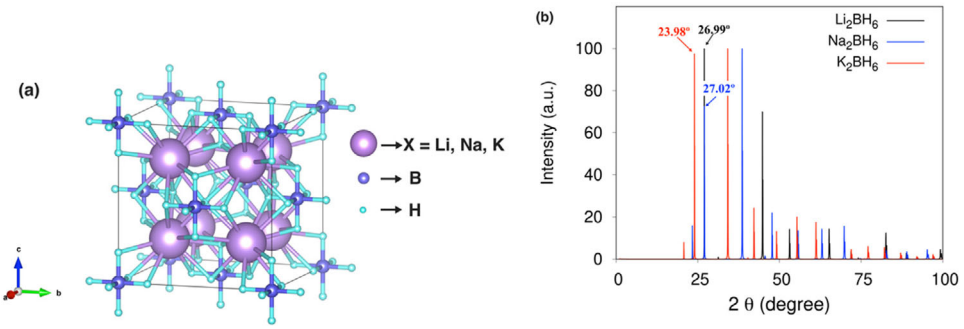


FIGURE 1 | (a) Crystal structure and (b) X-ray diffraction pattern for the X_2BH_6 (X = Li, Na, and K) double perovskite hydrides.

TABLE 1 | Lattice parameters (a in Å), unit cell volume (Å^3), formation energies (E_{for} in eV/atom), scattering angles (2θ) and Wyckoff positions for the X_2BH_6 (X = Li, Na, and K) double perovskite hydrides.

Compound	a (Å)	V (Å^3)	E_{for} (eV/atom)	2θ	Wyckoff positions
Li_2BH_6	5.72	186.95	−0.30	26.99°	Li: 8c (0.25, 0.25, 0.25) B: 4a (0.00, 0.00, 0.00) H: 24e (0.19, 0.00, 0.00)
Na_2BH_6	6.59	286.70	−0.28	27.02°	Na: 8c (0.25, 0.25, 0.25) B: 4a (0.00, 0.00, 0.00) H: 24e (0.21, 0.00, 0.00)
K_2BH_6	7.42	407.70	−0.42	23.98°	K: 8c (0.25, 0.25, 0.25) B: 4a (0.00, 0.00, 0.00) H: 24e (0.25, 0.00, 0.00)

The X_2BH_6 (X = Li, Na, and K) double perovskite hydrides crystallize in the cubic $Fm\bar{3}m$ space group (No. 225). The optimized crystal structure is illustrated in Figure 1a, wherein the X atoms occupy the 8c Wyckoff positions, the B atoms reside at the 4a sites, and the H atoms are located at the 24e sites. The optimized lattice parameters and Wyckoff coordinates are summarized in Table 1. A systematic increase in the lattice parameter is observed along the series Li_2BH_6 (5.72 Å) → Na_2BH_6 (6.59 Å) → K_2BH_6 (7.42 Å), which directly correlates with the increasing ionic radius of the alkali metal cation (Li^+: 0.76 Å, Na^+: 1.02 Å, K^+: 1.38 Å). It is evident from Table 1 that, as the lattice parameter increases, there is correspondingly an increase in the unit cell volume, resulting from a shift in position from the Li atom to the K atom. As these compositions have not been previously reported in the literature, direct comparison of the lattice parameters with prior studies is not possible.

The thermodynamic stability of each compound was assessed through the formation energy, calculated using Equation (1):

$$E_{for} = E_{Total(X_2BH_6)} - [2 * E(X) + E(B) + 3 * E(H_2)] \quad (1)$$

where $E_{Total\,(X_2BH_6)}$ is the total energy of the optimized X_2BH_6 unit cell, and $E(X)$, $E(B)$, and E (H_2) are the ground-state energies of the constituent elements of X and B and the energy of the hydrogen gas. As presented in Table 1, all three compounds exhibit negative formation energies: −0.30 eV/atom for Li_2BH_6, −0.28 eV/atom for Na_2BH_6, and −0.42 eV/atom for K_2BH_6. The negative formation energies confirm that these hydrides are thermodynamically stable with respect to their elemental constituents and are, in principle, amenable to experimental synthesis. Notably, K_2BH_6 exhibits the most negative formation energy, suggesting the highest thermodynamic driving force for formation among the three compounds.

From the standpoint of fundamental coordination chemistry, the existence of the BH_6 octahedral framework in the investigated X_2BH_6 series can be regarded as an unconventional state. In conventional complex metal hydrides, the presence of the highly stable tetrahedral tetrahidroborate (BH_4) configuration of boron is well established. The stabilization of a higher coordination number in these vacancy-ordered double perovskites closely mirrors the structural chemistry of Li_2BeH_6 analogues. In such systems, the extended hydrogen network is sustained by a delicate balance: strong covalent character within the localized polyanionic complex combined with long-range electrostatic stabilization provided by the surrounding alkali counter-ions (Li^+, Na^+ and K^+). However, transferring these promising computational properties into experimental reality poses undeniable synthesis challenges. It is evident that the presence of a high steric and electronic density surrounding the central boron atom results in the inherent metastability of the BH_6 sub-lattice under ambient conditions. The system exhibits a robust thermodynamic driving force that facilitates phase segregation into the prevalent alkali borohydride (XBH_4) and metal hydride (XH) phases. Consequently, the successful experimental synthesis of the pristine phase of X_2BH_6 would require the development and implementation of advanced, non-equilibrium synthetic methodologies. These include high-energy mechanical alloying (ball milling) under severe hydrogen overpressures, or ultra-

25130390, 2026, 9, Downloaded from https://advanced.onlinelibrary.wiley.com/doi/10.1002/adts.70534 by Turkey Cochrane Evidence Aid, Wiley Online Library on [31/08/2026]. See the Terms and Conditions (https://onlinelibrary.wiley.com/terms-and-conditions) on Wiley Online Library for rules of use; OA articles are governed by the applicable Creative Commons License

TABLE 2 | Gravimetric hydrogen storage capacity (C_{wt} %), volumetric hydrogen storage capacity (ρ_{vol} in g.H_2/L) and hydrogen desorption temperature (T_{des} in K) for the X_2BH_6 (X = Li, Na, and K) double perovskite hydrides.

Compound	C_{wt} %	ρ_{vol}	T_{des}
Li_2BH_6	19.71	214.88	218.77
Li_2SiH_6	12.60 [34]	142.25 [34]	107.78 [34]
Li_2BeH_6	20.00 [69]	48.14 [69]	673 [69]
Na_2BH_6	9.64	140.12	207.86
Na_2SiH_6	7.55 [34]	115.74 [34]	123.88 [34]
Na_2BeH_6	9.90 [69]	33.06 [69]	260 [69]
K_2BH_6	6.37	98.53	308.00
Mg_2SiH_6	7.31 [70]	—	496 [70]
Ca_2SiH_6	5.29 [70]	—	503 [70]
Sr_2SiH_6	2.89 [70]	—	511 [70]
Mg_2CrH_6	5.60 [71]	150.05 [71]	230.35 [71]
Mg_2MnH_6	5.51 [71]	142.07 [71]	208.65 [71]
Li@B14-40H_2	11.2 [72]	—	271 [72]
Na@a-C_5N_2+10H_2	9.0 [73]	—	189.19 [73]
Sc-decorated BO	10.96 [68]	81.49 [68]	319 [68]
Li@C_3N_2-12H_2	5.7 [74]	—	285 [74]
Na@B_5N_3 + 6H_2	7.80 [75]	—	299.00 [75]
Li@C18-12H_2	9.92 [76]	—	357 [76]

high-pressure stabilization via diamond anvil cells (DAC), similar to techniques utilized for exotic polyhydrides. It is imperative that researchers acknowledge this structural metastability if they are to successfully guide future experimental attempts aimed at synthesizing these ultra-high-capacity solid-state storage media.

To facilitate future experimental identification, the simulated X-ray diffraction patterns are presented in Figure 1b. The patterns exhibit characteristic peaks with maximum diffraction intensities at $2\theta = 26.99°$, 27.02°, and 23.98° for Li_2BH_6, Na_2BH_6, and K_2BH_6, respectively. The shift of the principal diffraction peaks to lower 2θ values with increasing lattice parameter is consistent with Bragg's law. The well-defined, sharp diffraction peaks indicate a high degree of crystalline ordering.

The gravimetric hydrogen storage capacity (C_{wt} %) was evaluated using Equation (2) [66].

$$C_{wt}\% = \left(\frac{\left(\frac{H}{M}\right) M_H}{M_{host} + \left(\frac{H}{M}\right) M_H} \times 100 \right)\% \quad (2)$$

where $\frac{H}{M}$ denotes the hydrogen-to-host atom ratio, M_H is the molar mass of hydrogen, and M_{host} is the molar mass of the host material. The calculated gravimetric capacities are listed in Table 2. Remarkably, all three hydrides exhibit high storage capacities: Li_2BH_6 achieves an exceptionally high value of 19.71 wt%, followed by Na_2BH_6 (9.64 wt%) and K_2BH_6 (6.37 wt%). The inverse relationship between the alkali metal atomic mass and the gravimetric capacity underscores the advantage of incorporating lightweight elements. All three compounds surpass the 2025 DOE target of 5.5 wt% for onboard hydrogen storage systems [67]. Furthermore, Li_2BH_6 and Na_2BH_6 exceed the DOE ultimate target of 6.5 wt%, while K_2BH_6 approaches this benchmark closely.

In order to further evaluate the practical feasibility of the investigated X_2BH_6 (X = Li, Na, and K) materials for use in onboard applications, the volumetric hydrogen storage capacities [34, 68] of the materials were calculated and compared with the targets set by the U.S. Department of Energy (DOE) [67]. Equation 3 was employed to obtain the volumetric hydrogen storage capacities where N_H is the number of absorbed hydrogen molecules, m_H is the molecular mass of hydrogen molecules, V is the volume of the unit cell and the N_A is the Avogadro's number [34]. In this regard, the US DOE (United States Department of Energy) has established volumetric storage capacity targets of 40 g/L for the year 2025 and 50 g/L for long-term ultimate goals [67]. The findings, presented in Table 2, demonstrate that all three studied structures exhibit substantial performance superiority to these targets. The material under consideration, Li_2BH_6, has been found to exhibit an exceptional volumetric hydrogen density of 214.88 g.H_2/L, a figure that exceeds the ultimate DOE requirement by more than fourfold. As the alkali metals (Li, Na, and K) are considered, it is observed that the volumetric capacity decreases due to the expansion of the unit cell volume. However, the values for both Na_2BH_6 (140.12 g.H_2/L) and K_2BH_6 (98.53 g.H_2/L) are greater than the ultimate threshold, indicating stability in these compounds. These results indicate that the materials investigated herein possess excellent volumetric efficiency. It can thus be concluded that the materials under consideration are highly promising candidates for use in compact solid-state hydrogen storage systems that exhibit high density.

$$\rho_{vol} = \frac{N_H \times m_H}{V \times N_A} \quad (3)$$

The hydrogen desorption temperature (T_{des}) at 1 bar equilibrium pressure was estimated using the van't Hoff relation (Equation 4) [67, 77]:

$$\Delta H = T \times \Delta S \quad (4)$$

where ΔH is the formation enthalpy per hydrogen molecule and ΔS is the entropy change associated with the transition from solid-state hydrogen to gaseous H_2, taken as 130.7 J/(mol·K) [67, 77]. Here, the desorption enthalpy (ΔH) is directly evaluated from the formation enthalpy (E_{for}) of the double perovskite hydrides relative to the molecular H_2 gas reference state, assuming a complete decomposition back into the constituent elements. It should be noted that this approach employs a constant entropy approximation and uses the total formation enthalpy as a proxy for the dehydrogenation enthalpy, which represents a simplification; the actual desorption thermodynamics may vary depending on the specific decomposition pathway. The DOE has established a target operating temperature range of 233–333 K [67]. As shown in Table 2, K_2BH_6 exhibits a desorption temperature of 308.00 K, which falls within the DOE target range. In contrast, Li_2BH_6 (218.77 K) and Na_2BH_6 (207.86 K) exhibit desorption temperatures

25130390, 2026, 9, Downloaded from https://advanced.onlinelibrary.wiley.com/doi/10.1002/adts.70534 by Turkey Cochrane Evidence Aid, Wiley Online Library on [31/08/2026]. See the Terms and Conditions (https://onlinelibrary.wiley.com/terms-and-conditions) on Wiley Online Library for rules of use; OA articles are governed by the applicable Creative Commons License

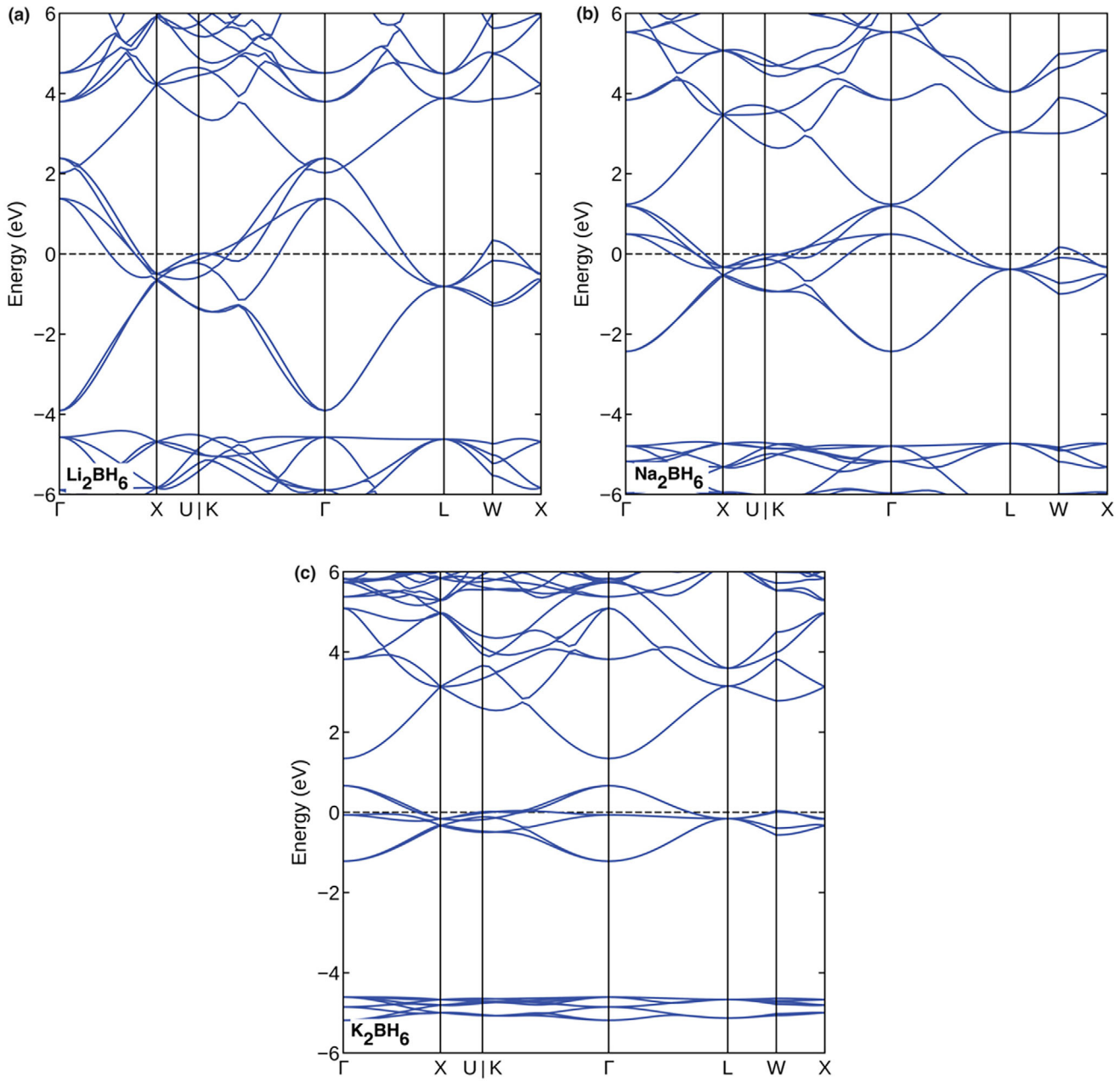


FIGURE 2 | Electronic band structures obtained using the GGA-PBE method for (a) Li_2BH_6, (b) Na_2BH_6, and (c) K_2BH_6 double perovskite hydrides.

below this range, suggesting that maintaining hydrogen in the stored state may require sub-ambient conditions. A comprehensive evaluation of hydrogen storage viability must also consider the mechanical and dynamical stability of the host material, as discussed in the following sections.

While it is well-established that phase stability is dictated by thermodynamic properties, they also provide critical indirect indicators with regard to the kinetic recovery time of hydrogen storage systems [68]. In the present study, the calculated hydrogen desorption temperatures (T_{des}) for the investigated series X_2BH_6 are found to be remarkably favorable. The T_{des} for Li_2BH_6 was calculated as 218.77 K, while that for Na_2BH_6 was found to be 207.86 K. For K_2BH_6, the T_{des} was determined to be 308.00 K. In the context of solid-state kinetics, the observation of low-to-moderate T_{des} values suggests that the activation energy barriers required for hydrogen recombination and desorption are relatively low. Consequently, the systems are expected to exhibit rapid desorption rates and short recovery times under practical working conditions without suffering from the sluggish kinetic bottlenecks typical of conventional high-temperature hydrides.

In order to provide a clear context and to emphasize the enhanced performance of the investigated X_2BH_6 (X = Li, Na, and K) double perovskite hydrides, a comprehensive horizontal and vertical benchmarking study was conducted against prominent hydrogen storage candidates from recent literature. When evaluated along the vertical axis, relative to sister perovskite-type silicides (for instance, M_2SiH_6 where M represents Li, Na, Mg, Ca, Sr), the boron-based X_2BH_6 series demonstrates a considerable

25130390, 2026, 9, Downloaded from https://advanced.onlinelibrary.wiley.com/doi/10.1002/adts.70534 by Turkey Cochrane Evidence Aid, Wiley Online Library on [31/08/2026]. See the Terms and Conditions (https://onlinelibrary.wiley.com/terms-and-conditions) on Wiley Online Library for rules of use; OA articles are governed by the applicable Creative Commons License

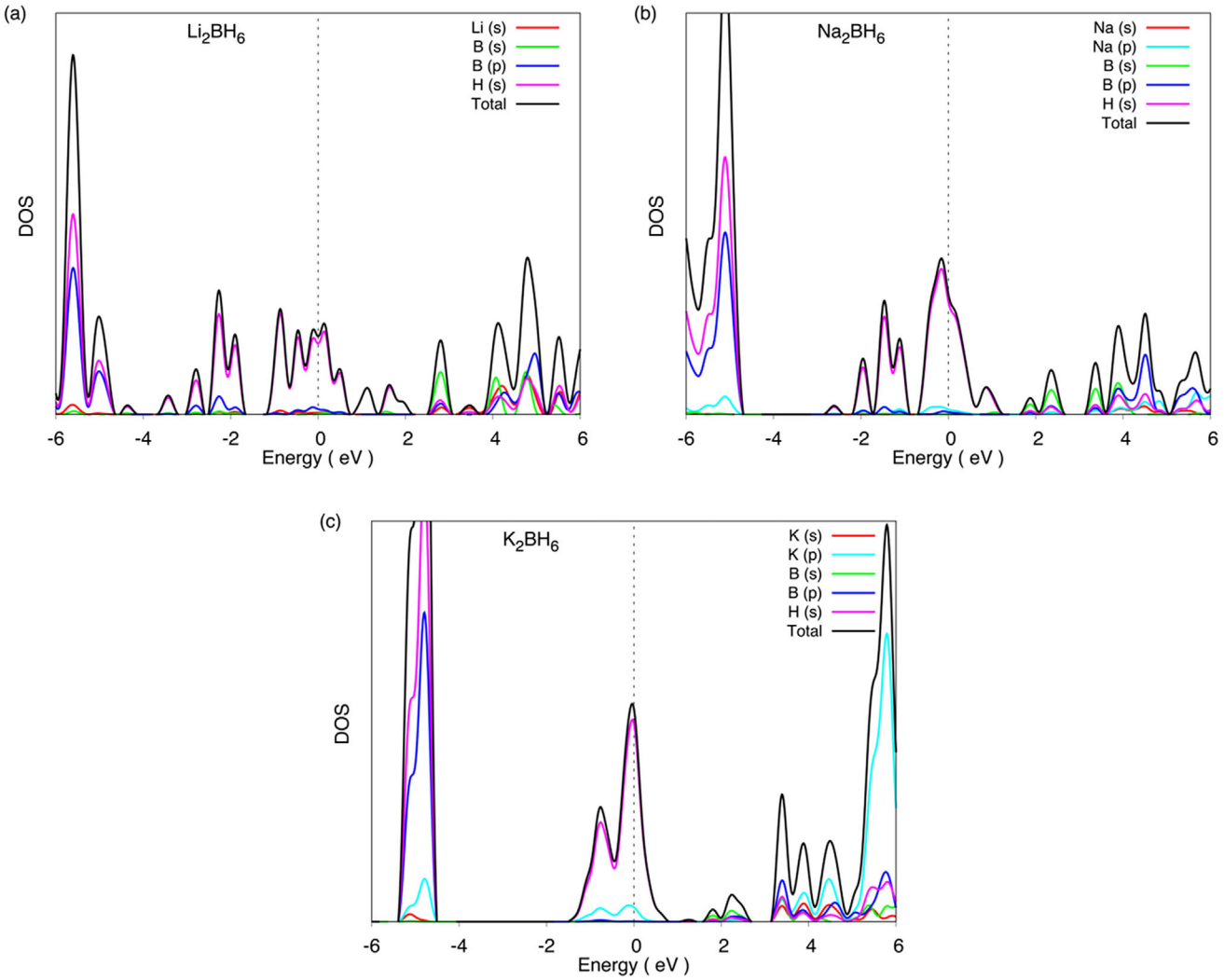


FIGURE 3 | Electronic density of states obtained using the PBE method for (a) Li_2BH_6, (b) Na_2BH_6, and (c) K_2BH_6 double perovskite hydrides.

advantage. Specifically, the gravimetric capacity of Li_2BH_6 is 19.71 wt.%, representing an extraordinary volumetric density of 214.88 g/L, which significantly exceeds that of Li_2SiH_6 (12.60 wt.%, 142.25 g/L) [34]. Moreover, the gravimetric capacity of Li_2BeH_6 has been shown to be comparable (20.00 wt.%), its potential practical applications are hindered by its low volumetric capacity (48.14 g/L) and a desorption temperature (T_{des} = 673 K) that is too high to be considered useful [69]. In contrast, the proposed X_2BH_6 structures deliver well-balanced thermodynamics with T_{des} values operating in highly accessible regimes (207.86–308.00 K). Horizontally, the investigated systems were evaluated against state-of-the-art 2D nanomaterials and decorated carbon/boron-nitride networks (α C_3N_2 [74], B_5N_3 [75],C18 [76] and B14 [72]). Although the decoration of lithium or sodium atoms on two-dimensional templates can yield gravimetric capacities of between 5.70 and 11.20 wt.%, the inherent issue with open-surface topologies is that there is frequently an absence of data regarding the reported volumetric packing densities. The double-perovskite matrix of X_2BH_6 has been demonstrated to successfully bridge this gap, combining ultra-high volumetric densities with gravimetric metrics that are competitive with, or even exceed, those of the finest 2D storage platforms. This comprehensive cross-comparison unambiguously underscores the exceptional promise of the studied double perovskites for high-density solid-state hydrogen storage.

3.2 | Electronic Properties

Understanding the electronic structure of hydrogen storage materials is essential for elucidating the nature of chemical bonding and charge transfer mechanisms that govern hydrogen uptake and release. Figure 2 presents the electronic band structures of the X_2BH_6 compounds along the high-symmetry directions of the first Brillouin zone, computed using the GGA-PBE functional. All three hydrides exhibit metallic character, as evidenced by electronic bands crossing the Fermi level. The metallic character is associated with high electronic conductivity, which may facilitate rapid charge transfer processes relevant to hydrogen absorption and desorption kinetics [66, 77].

It is pertinent to note that the GGA-PBE functional is well established to systematically underestimate electronic bandgaps in solids, with typical deviations of 40–50% relative to experimental values [78]. Consequently, the metallic behavior predicted at the PBE level may, in some cases, correspond to a narrow-gap

25130390, 2026, 9, Downloaded from https://advanced.onlinelibrary.wiley.com/doi/10.1002/adts.70534 by Turkey Cochrane Evidence Aid, Wiley Online Library on [31/08/2026]. See the Terms and Conditions (https://onlinelibrary.wiley.com/terms-and-conditions) on Wiley Online Library for rules of use; OA articles are governed by the applicable Creative Commons License

TABLE 3 | Bader charges (in units of e) for the X_2BH_6 (X = Li, Na, and K) double perovskite hydrides.

Compound	X	B	H
Li_2BH_6	7.02	4.38	−11.41
Na_2BH_6	6.76	4.60	−11.36
K_2BH_6	6.07	4.83	−10.91

TABLE 4 | Elastic constants (C_{ij} in GPa) for the X_2BH_6 (X = Li, Na, and K) double perovskite hydrides.

Compound	C_{11}	C_{12}	C_{44}
Li_2BH_6	91.45	73.34	55.73
Na_2BH_6	23.95	50.71	19.98
K_2BH_6	30.76	19.66	6.66

TABLE 5 | Bulk modulus (B in GPa), shear modulus (G in GPa), Young's modulus (E in GPa), Poisson's ratio (ν), G/B and B/G ratios for the X_2BH_6 (X = Li and K) double perovskite hydrides.

Compound	B	G	E	ν	G/B	B/G
Li_2BH_6	79.38	27.63	74.27	0.34	0.35	2.87
K_2BH_6	23.36	6.19	17.06	0.38	0.27	3.77

semiconducting state when computed with higher-level methods such as the HSE06 screened hybrid functional or GW many-body perturbation theory. Nevertheless, the qualitative conclusion of high electronic conductivity is consistent with the metallic bonding character inferred from the mechanical property analysis (Section 3.3). Future investigations employing hybrid functionals are recommended to establish a more precise characterization of the electronic nature of these materials.

The partial and total electronic densities of states (DOS) are presented in Figure 3. The DOS profiles corroborate the metallic character, with a finite density of states at the Fermi level (E_F) for all three compounds. The dominant contribution to the DOS at E_F originates from the H-1s orbitals, indicating that the hydrogen sublattice plays a central role in determining the electronic properties near the Fermi level. In the energy range of −4 to −6 eV below E_F, hybridization between the B-2p and H-1s orbitals is observed, which is indicative of covalent B—H bonding within the $[BH_6]^{5-}$ octahedral units. In the conduction band region (4–6 eV above E_F), the primary contributions arise from the X-*s* and X-*p* orbitals, along with the B-2p states.

To quantify the charge redistribution, Bader charge analysis was performed, and the results are summarized in Table 3. The values represent cumulative Bader charges summed over all atoms of each element type within the X_2BH_6 formula unit (i.e., 2 X atoms, 1 B atom, and 6 H atoms). Positive values indicate net electron depletion, while negative values signify net electron accumulation [79]. The X and B atoms exhibit positive Bader charges (electron donors), while the H atoms accumulate negative charge (electron acceptors). This charge transfer pattern is consistent with the ionic character of the X–H interactions and the partially covalent B—H bonding. The magnitude of charge transfer from the X site decreases from Li (7.02*e*) to Na (6.76*e*) to K (6.07*e*), while the charge donated by B increases from 4.38 to 4.60 to 4.83*e*, suggesting a progressive strengthening of the B–H interaction as the alkali metal becomes heavier.

3.3 | Mechanical Properties

The elastic stiffness constants were computed using the stress–strain method, and the results are listed in Table 4. Mechanical stability was assessed against the Born–Huang criteria [80, 81] for cubic crystals (Equation 5):

$$C11 > 0, C44 > 0, C11 - C12 > 0, C11 + 2C12 > 0 \quad (5)$$

Li_2BH_6 satisfies all four conditions and is mechanically stable. K_2BH_6 likewise fulfills the Born criteria, though with considerably smaller elastic constants reflecting a softer lattice. Critically, Na_2BH_6 violates the tetragonal shear stability condition ($C_{11} - C_{12} = 23.95 - 50.71 = -26.76$ GPa < 0), rendering it mechanically unstable against tetragonal distortion. This instability implies that the cubic $Fm\bar{3}m$ phase of Na_2BH_6 is not mechanically viable and may undergo spontaneous distortion to a lower-symmetry structure. Consequently, subsequent mechanical analysis is restricted to Li_2BH_6 and K_2BH_6.

Table 5 lists the Bulk modulus, shear modulus, Young's modulus, Poisson's ratio, G/B and B/G ratios for the X_2BH_6 (X = Li and K) double perovskite hydrides. The bulk modulus is substantially higher for Li_2BH_6 (79.38 GPa) than for K_2BH_6 (23.36 GPa), indicating a significantly more incompressible lattice. The shear modulus follows the same trend: 27.63 GPa for Li_2BH_6 vs. 6.19 GPa for K_2BH_6. Young's modulus is 74.27 and 17.06 GPa for Li_2BH_6 and K_2BH_6, respectively. The progressive softening reflects the weaker interatomic interactions associated with the larger, more electropositive K cation.

The Poisson's ratio (ν) serves as an indicator of bonding character: values near 0.1 are characteristic of covalent materials, values near 0.25 indicate predominantly ionic bonding, and values approaching 0.33 or higher are typical of metallic bonding [79, 82].

TABLE 6 | Longitudinal (V_l in m/s), transverse (V_t in m/s) and average wave velocities (V_m in m/s), Debye temperature (θ_D in K), anisotropic factor A for the X_2BH_6 (X = Li and K) double perovskite hydrides.

Compound	V_l	V_t	V_m	θ_D	A
Li_2BH_6	10678.76	5206.48	5849.05	982.70	6.16
K_2BH_6	4547.59	2012.44	2271.32	299.80	1.20

25130390, 2026, 9, Downloaded from https://advanced.onlinelibrary.wiley.com/doi/10.1002/adts.70534 by Turkey Cochrane Evidence Aid, Wiley Online Library on [31/08/2026]. See the Terms and Conditions (https://onlinelibrary.wiley.com/terms-and-conditions) on Wiley Online Library for rules of use; OA articles are governed by the applicable Creative Commons License

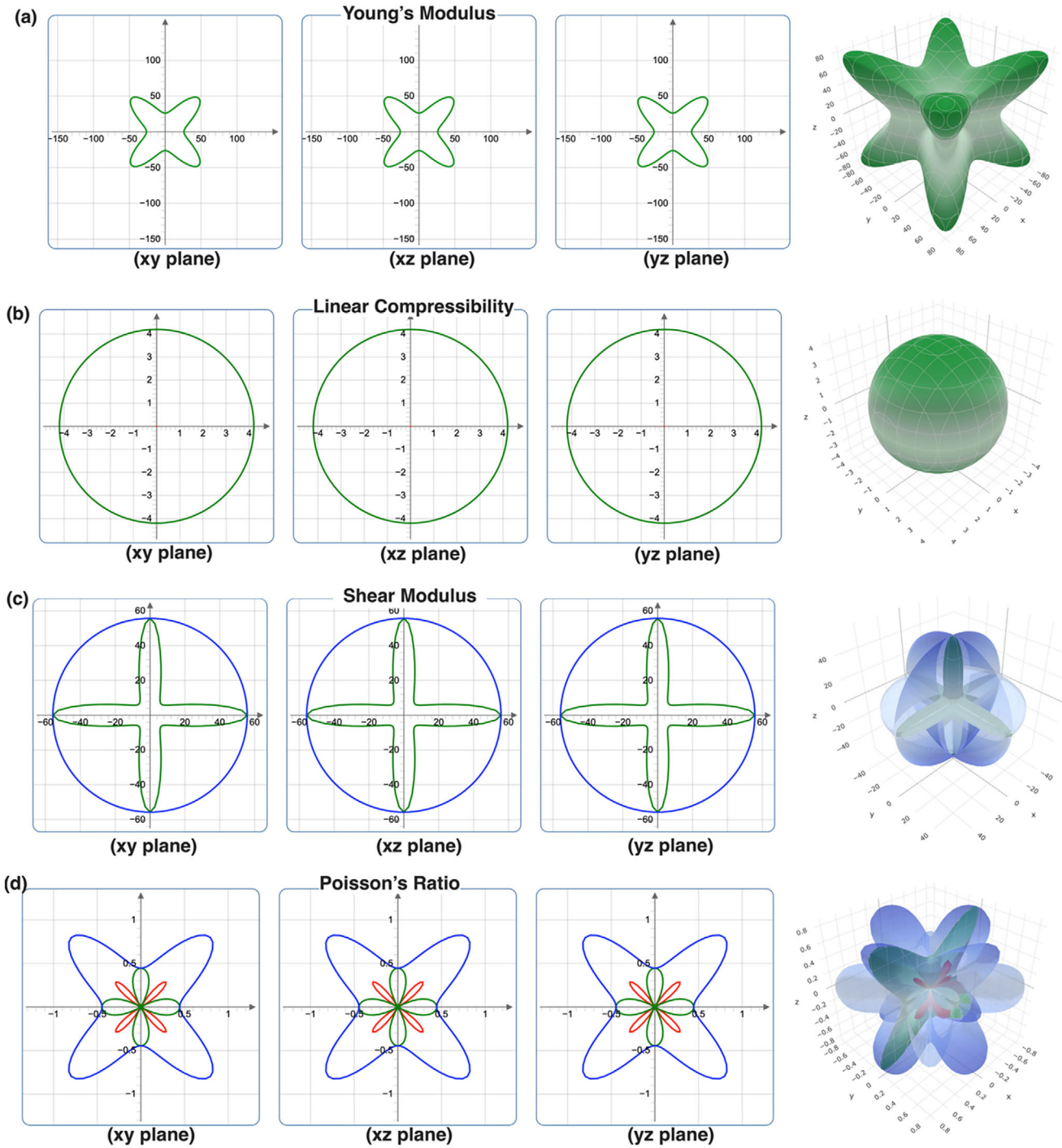


FIGURE 4 | 2D and 3D visualizations of the (a) Young's modulus, (b) linear compressibility, (c) shear modulus and (d) Poisson's ratio for Li_2BH_6.

In agreement with the electronic structure analysis, the Poisson's ratios for both Li_2BH_6 ($\nu = 0.34$) and K_2BH_6 ($\nu = 0.38$) exceed 0.33, indicating the presence of predominantly metallic bonding. The G/B ratios of 0.35 and 0.27 corroborate this finding [82].

The ductile vs. brittle nature was assessed using Pugh's criterion [83]: B/G > 1.75 indicates ductile behavior. With B/G values of 2.87 and 3.77, both compounds are classified as ductile. Additionally, the Cauchy pressure ($C_{12} - C_{44}$) provides further bonding insight via Pettifor's criterion [84]: positive values suggest metallic/ionic bonding with ductile response. For Li_2BH_6, $C_{12} - C_{44} = +17.61$ GPa, and for K_2BH_6, $C_{12} - C_{44} = +13.00$ GPa; both positive, confirming the ductile metallic nature. The ductility of these materials is favorable for hydrogen storage, implying greater resistance to mechanical degradation during repeated hydrogenation/dehydrogenation cycles.

The mechanical investigation of Li_2BH_6 and K_2BH_6 was extended by evaluating their Debye temperatures and anisotropic elastic properties. Following the methodologies in references [66, 85], the Debye temperature (θ_D), average wave velocity (V_m), longitudinal wave velocity (V_l), and transverse wave velocity (V_t)

25130390, 2026, 9, Downloaded from https://advanced.onlinelibrary.wiley.com/doi/10.1002/adts.70534 by Turkey Cochrane Evidence Aid, Wiley Online Library on [31/08/2026]. See the Terms and Conditions (https://onlinelibrary.wiley.com/terms-and-conditions) on Wiley Online Library for rules of use; OA articles are governed by the applicable Creative Commons License

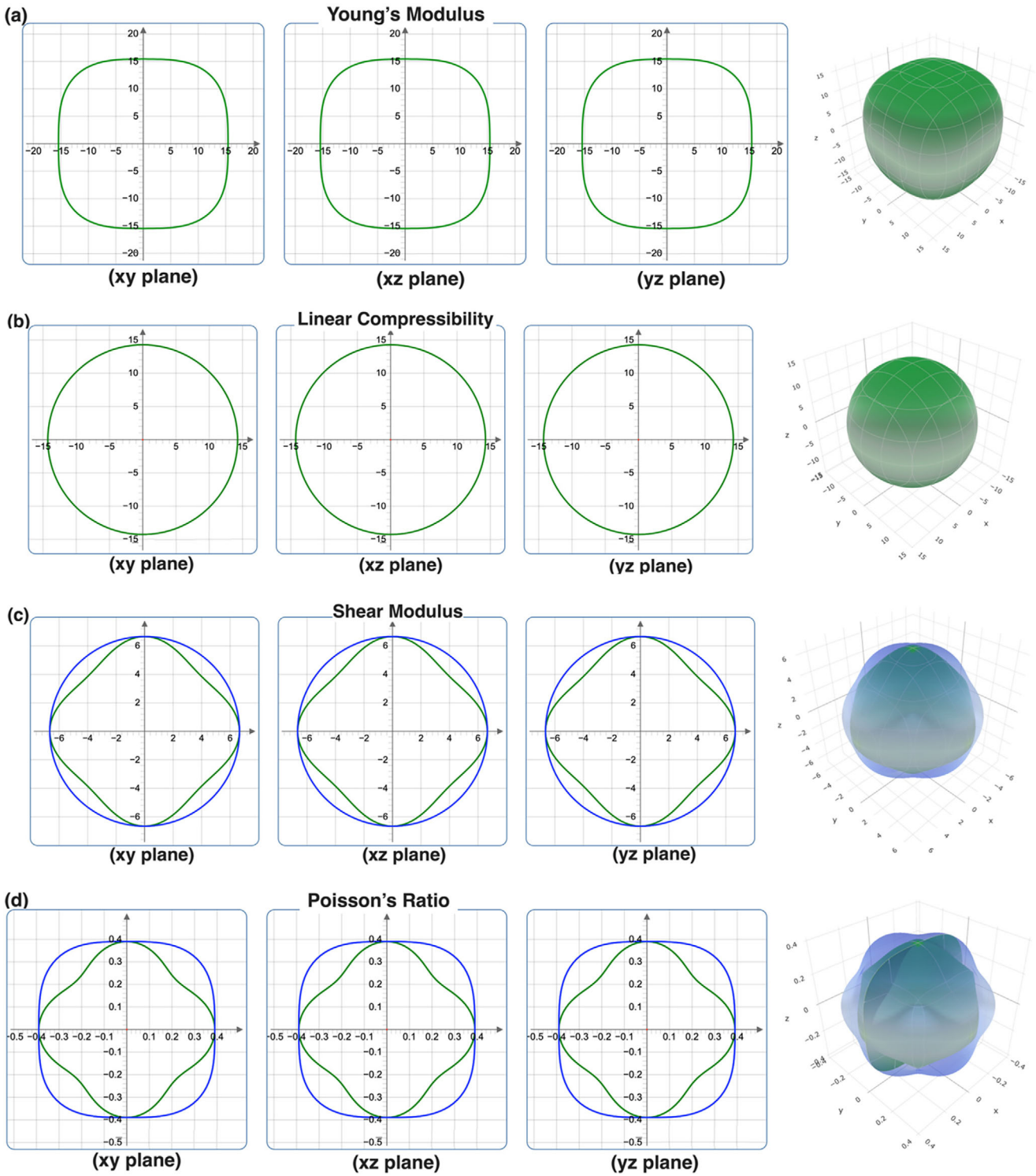


FIGURE 5 | 2D and 3D visualizations of the (a) Young's modulus, (b) linear compressibility, (c) shear modulus and (d) Poisson's ratio for K_2BH_6.

were calculated. Due to the inherent crystal symmetry of these cubic structures, the primary anisotropic factors ($A1$, $A2$, and $A3$) are identical, which allows the material's anisotropy to be represented by a single anisotropic factor (A). An A value of unity indicates an isotropic material, while any deviation from this value signifies anisotropic behavior. These findings, including the anisotropic factors calculated via the equation in reference [86], are summarized in Table 6. Notably, the Debye temperature is significantly higher for Li_2BH_6 (982.70 K) than for K_2BH_6 (299.80 K), indicating stronger interatomic bonding and higher thermal conductivity. Li_2BH_6 exhibits pronounced elastic anisotropy (A = 6.16), while K_2BH_6 is nearly isotropic (A = 1.20).

The direction-dependent elastic properties were visualized using the ELATE software [87], as shown in Figures 4 and 5. For both compounds, the linear compressibility is isotropic, con-

25130390, 2026, 9, Downloaded from https://advanced.onlinelibrary.wiley.com/doi/10.1002/adts.70534 by Turkey Cochrane Evidence Aid, Wiley Online Library on [31/08/2026]. See the Terms and Conditions (https://onlinelibrary.wiley.com/terms-and-conditions) on Wiley Online Library for rules of use; OA articles are governed by the applicable Creative Commons License

TABLE 7 | The maximum and minimum values of the Young's modulus (E), linear compressibility (β), shear modulus (G) and Poisson's ratio ν for the X_2BH_6 (X = Li and K) double perovskite hydrides.

Compound	E (GPa)		β (TPa^{-1})		G (GPa)		ν	
	E_{min}	E_{max}	β_{min}	β_{max}	G_{min}	G_{max}	ν_{min}	ν_{max}
Li_2BH_6	26.17	135.48	4.20	4.20	9.06	55.73	−0.41	1.13
K_2BH_6	15.43	18.25	14.27	14.27	5.55	6.66	0.31	0.44

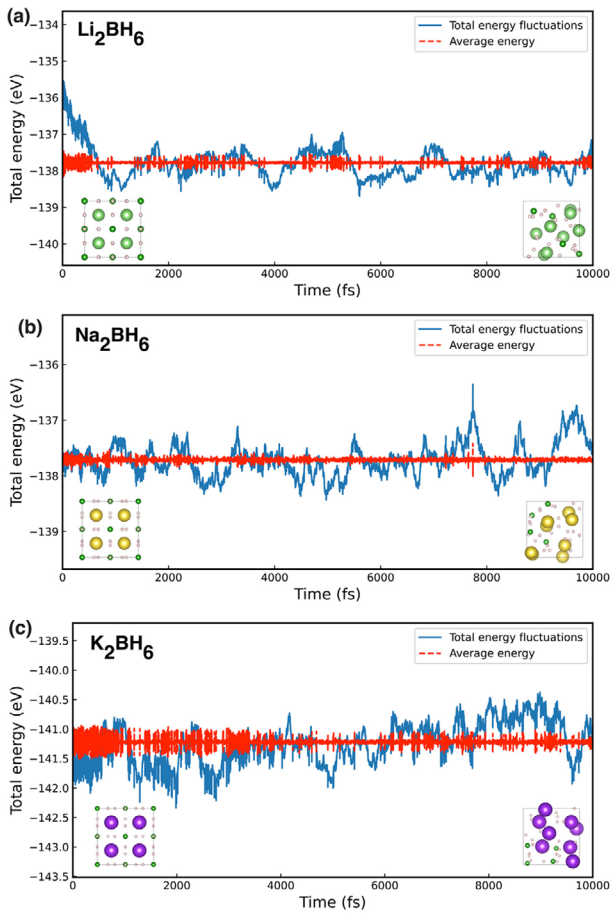


FIGURE 6 | Total energy change throughout the AIMD simulations for (a) Li_2BH_6, (b) Na_2BH_6, and (c) K_2BH_6.

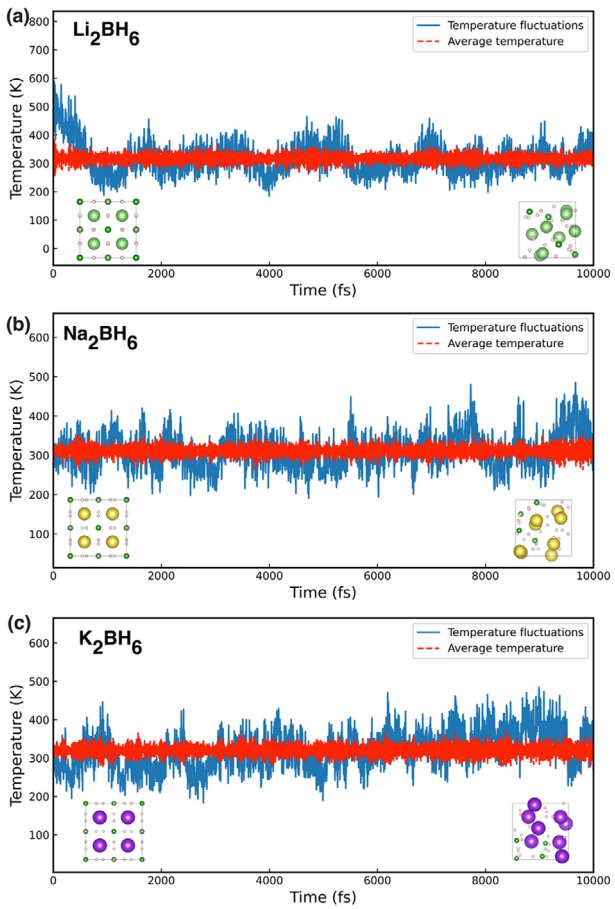


FIGURE 7 | Temperature change throughout the AIMD simulations for (a) Li_2BH_6, (b) Na_2BH_6, and (c) K_2BH_6.

sistent with cubic symmetry. However, the Young's modulus, shear modulus, and Poisson's ratio exhibit varying degrees of directional dependence (Table 7). It is particularly noteworthy that Li_2BH_6 displays a negative minimum Poisson's ratio (−0.41). This signifies auxetic behavior along specific crystallographic directions, a characteristic that could influence the mechanical stability of the material during the volumetric shifts inherent in hydrogen cycling.

3.4 | Ab-Inito Molecular Dynamic and Lattice Dynamical Properties

Ab-Initio molecular dynamics (AIMD) calculations were used to obtain the thermodynamic stability of X_2BH_6 (X = Li, Na, and K) double perovskite hydrides. To this end, machine learning force fields were utilized to accelerate the AIMD calculations. Figures S1–S3 illustrate the Bayesian error of the MLFF along with the root mean square error (RMSE) of the forces for the Li_2BH_6, Na_2BH_6, and K_2BH_6, respectively. As demonstrated in the figures, both the Bayesian error and the root mean square error (RMSE) value of the forces are small, indicating that the model has been well trained and is suitable for accurate AIMD calculations. The total energy and temperature changes over 10 000 fs during AIMD calculations for the X_2BH_6 double perovskite hydrides are shown in Figures 6 and 7, respectively. The material's thermodynamic stability at 300 K is confirmed by the minimal fluctuations in both total energy and temperature. Figures 6 and 7 also show the initial and final crystal structures, which display no significant changes. As a result of these simulations, the thermodynamic stability of the X_2BH_6 double perovskite hydrides has been confirmed by the AIMD studies.

25130390, 2026, 9, Downloaded from https://advanced.onlinelibrary.wiley.com/doi/10.1002/adts.70534 by Turkey Cochrane Evidence Aid, Wiley Online Library on [31/08/2026]. See the Terms and Conditions (https://onlinelibrary.wiley.com/terms-and-conditions) on Wiley Online Library for rules of use; OA articles are governed by the applicable Creative Commons License

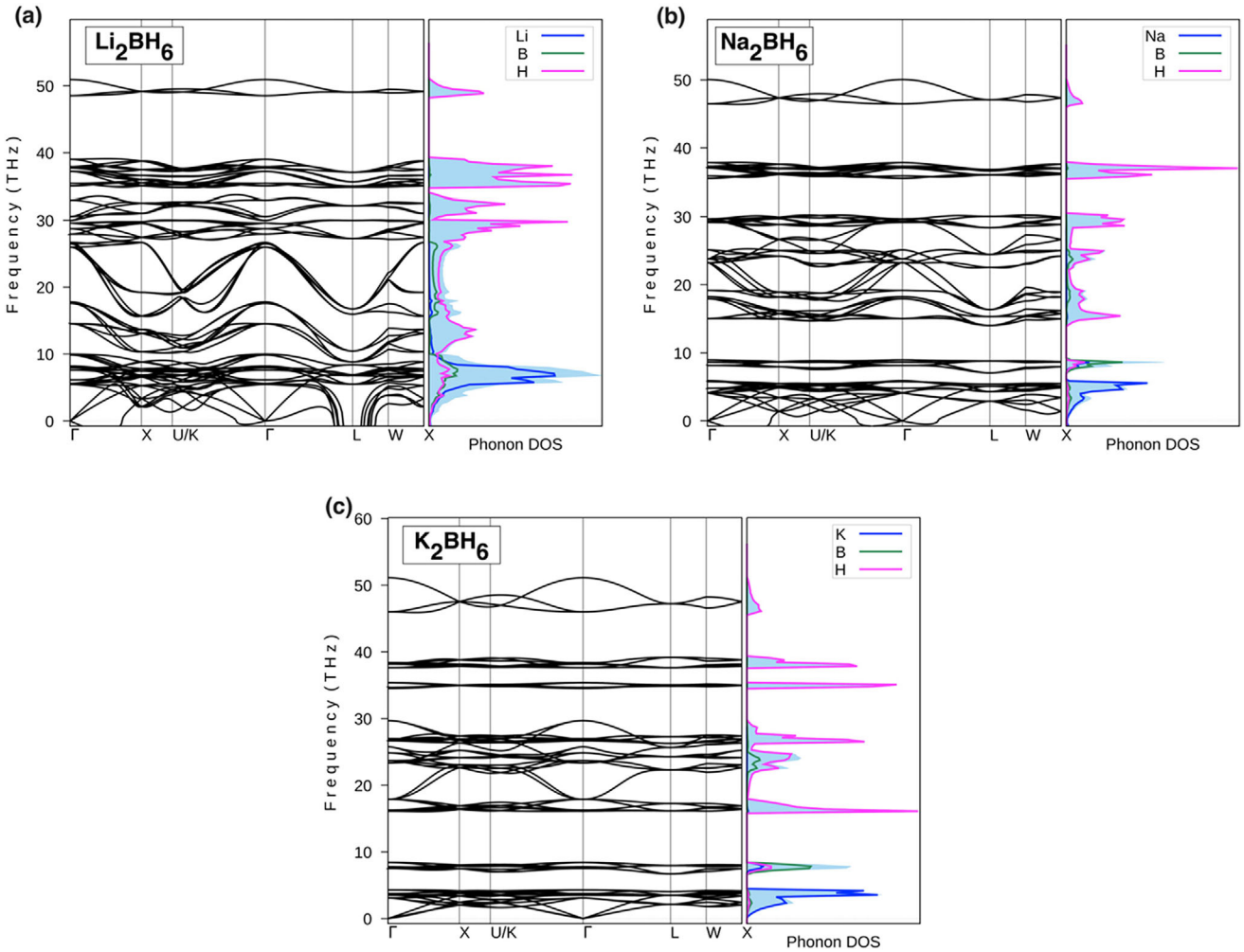


FIGURE 8 | The phonon dispersion curves for (a) Li_2BH_6, (b) Na_2BH_6, and (c) K_2BH_6.

Lattice dynamical stability is a necessary condition for the physical realizability of a crystalline compound at finite temperatures. The phonon dispersion curves computed via the finite displacement method with 2×2×2 supercells are presented in Figure 8. With 9 atoms per primitive unit cell, each dispersion diagram comprises 3 acoustic and 24 optical branches.

The phonon dispersion of K_2BH_6 (Figure 8c) shows exclusively positive frequencies throughout the Brillouin zone, confirming its dynamical stability. This result, combined with its negative formation energy and satisfaction of the Born criteria, establishes K_2BH_6 as a comprehensively stable compound. In contrast, both Li_2BH_6 and Na_2BH_6 exhibit imaginary phonon frequencies, indicating dynamical instability. The presence of soft phonon modes implies that the cubic $Fm\bar{3}m$ structure represents a saddle point rather than a true minimum on the potential energy surface for these two compositions. These materials may potentially be stabilized in lower-symmetry phases, at elevated temperatures through anharmonic effects, or via compositional modifications, which warrants further investigation.

The phonon density of states reveals a characteristic frequency separation: high-frequency modes (above ~30 THz) are predominantly associated with H atom vibrations, while the low-frequency region is dominated by the heavier X and B atoms. This separation is a common feature of metal hydrides arising from the large mass contrast between hydrogen and the remaining constituents.

The thermodynamic functions derived from the phonon calculations are presented in Figure 9. The temperature-dependent free energy, entropy, and heat capacity exhibit the expected behavior: entropy and heat capacity increase monotonically with temperature, while the Helmholtz free energy decreases. At high temperatures, the heat capacity asymptotically approaches the Dulong–Petit classical limit. The thermodynamic functions for Li_2BH_6 and Na_2BH_6 are computed under the harmonic approximation for structures that are not true energy minima, and should be interpreted with appropriate caution.

4 | Conclusion

This comprehensive first principles investigation using density functional theory within the GGA PBE framework has successfully characterized the structural, electronic, mechanical, and hydrogen storage properties of X_2BH_6 (X = Li, Na, and K) double perovskite hydrides. The results indicate that while

25130390, 2026, 9, Downloaded from https://advanced.onlinelibrary.wiley.com/doi/10.1002/adts.70534 by Turkey Cochrane Evidence Aid, Wiley Online Library on [31/08/2026]. See the Terms and Conditions (https://onlinelibrary.wiley.com/terms-and-conditions) on Wiley Online Library for rules of use; OA articles are governed by the applicable Creative Commons License

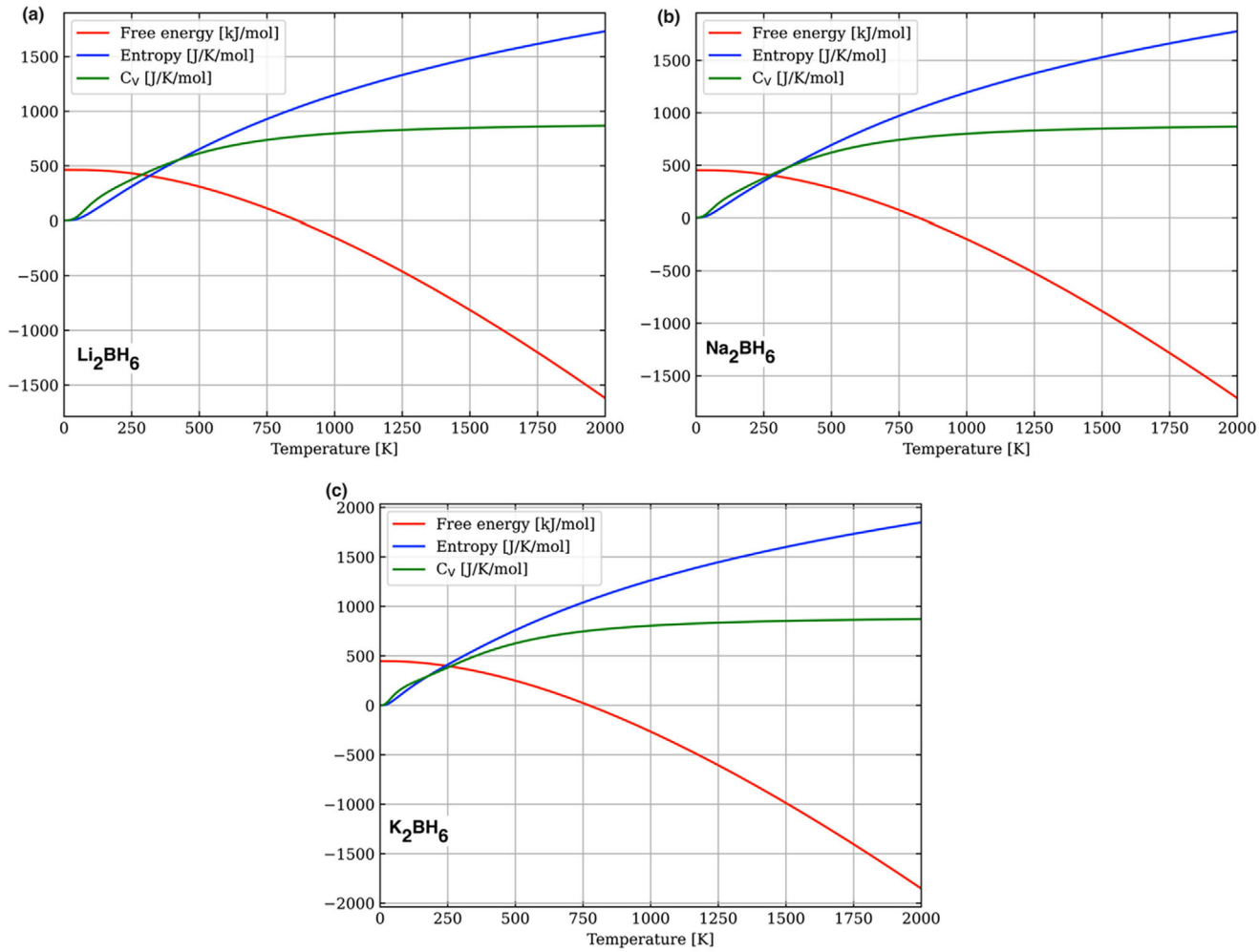


FIGURE 9 | The temperature dependent heat capacity, entropy and free energy for (a) Li_2BH_6, (b) Na_2BH_6, and (c) K_2BH_6.

all three hydrides are thermodynamically stable with negative formation energies, only Li_2BH_6 and K_2BH_6 satisfy the Born Huang criteria for mechanical stability. Furthermore, phonon dispersion calculations identify K_2BH_6 as the only compound that is simultaneously stable in thermodynamic, mechanical, and dynamic terms.

The gravimetric hydrogen storage capacities of these materials are exceptionally high at 19.71, 9.64, and 6.37 wt% for Li_2BH_6, Na_2BH_6, and K_2BH_6 respectively, all of which significantly exceed the 2025 DOE target of 5.5 wt%. Detailed mechanical analysis shows that the substitution of Li with K results in a notable decrease in both wave velocities and the Debye temperature, with K_2BH_6 exhibiting a θ_D of 299.80 K compared to 982.70 K for Li_2BH_6. Due to the inherent cubic crystal symmetry, the anisotropic factors $A1$, $A2$, and $A3$ are identical and are consequently represented by a single anisotropic factor A in the reported findings.

Ultimately, K_2BH_6 emerges as the most promising candidate for practical energy applications because it combines total structural stability with a desorption temperature of 308.00 K which falls within the DOE target operating range of 233 to 333 K. While operating near ambient temperatures is highly desirable for onboard solid-state hydrogen storage applications, claiming immediate practical viability for K_2BH_6 requires careful qualification. The higher T_{des} of the potassium variant relative to its lithium and sodium counterparts implies a stronger chemical binding within the vacancy-ordered sub-lattice. From a kinetic perspective, this increased stability often correlates with higher activation energy barriers for the nucleation and growth of desorbed phases, which could slow down the hydrogen release kinetics in practice. Furthermore, the complete multi-step decomposition pathway might involve competing intermediate amorphous or binary phases that could alter the net operating pressures. Therefore, while K_2BH_6 stands out as a promising candidate from a purely capacity and equilibrium thermodynamic standpoint, its ultimate technical viability remains subject to thorough future verification of its kinetic barriers and phase stability under cyclic operating conditions.

Author Contributions

Aysenur Gencer: Writing – original draft, Validation, Methodology, Conceptualization. Ahmet Aydogan: Writing – original draft, Investigation, Data curation. Ozge Surucu: Writing – original draft, Investigation, Conceptualization. Gokhan Surucu: Writing – review & editing, Validation, Supervision, Methodology, Funding acquisition, Conceptualization.

25130390, 2026, 9, Downloaded from https://advanced.onlinelibrary.wiley.com/doi/10.1002/adts.70534 by Turkey Cochrane Evidence Aid, Wiley Online Library on [31/08/2026]. See the Terms and Conditions (https://onlinelibrary.wiley.com/terms-and-conditions) on Wiley Online Library for rules of use; OA articles are governed by the applicable Creative Commons License

Acknowledgements

The numerical calculations were performed using TRUBA resources at TUBITAK ULAKBIM, High Performance and Grid Computing Centre, and at Istanbul Technical University National Center for High-Performance Computing.

Use of Generative AI and AI-Assisted Technologies in the Writing Process

During the preparation of this work the authors used Google Gemini in order to enhance the language, clarity, and overall readability of the manuscript. After using this tool/service, the authors reviewed and edited the content as needed and take full responsibility for the content of the published article.

Conflicts of Interest

None of the authors have a conflict of interest to disclose.

Data Availability Statement

The data that support the findings of this study are available from the corresponding author upon reasonable request.

References

1. M. Ali, Q. Ain, M. Alkadi, et al., "First-Principles Evaluation of $LiCaF_{3-\alpha}H_{\alpha}$ as an Effective Material for Solid-State Hydrogen Storage," *Journal of Energy Storage* 83 (2024): 110731, https://doi.org/10.1016/j.est.2024.110731.

2. N. Ma, W. Zhao, W. Wang, X. Li, and H. Zhou, "Large Scale of Green Hydrogen Storage: Opportunities and Challenges," *International Journal of Hydrogen Energy* 50 (2024): 379–396, https://doi.org/10.1016/j.ijhydene.2023.09.021.

3. N. F. Attia, S. E. A. Elashery, M. A. Nour, et al., "Recent Advances in Sustainable and Efficient Hydrogen Storage Nanomaterials," *Journal of Energy Storage* 100 (2024): 113519, https://doi.org/10.1016/j.est.2024.113519.

4. C. B. B. Farias, R. C. S. Barreiros, M. F. da Silva, et al., "Use of Hydrogen as Fuel: A Trend of the 21st Century," *Energies* 15 (2022): 311, https://doi.org/10.3390/EN15010311.

5. Y. Didi, Z. El Fatouaki, R. Touti, et al., "First Principles Computational Study of MgX_3H_8 (X = V and Fe) for Hydrogen Storage Applications," *International Journal of Hydrogen Energy* 133 (2025): 140–151, https://doi.org/10.1016/j.ijhydene.2025.04.265.

6. L. Mulky, S. Srivastava, T. Lakshmi, et al., "An Overview of Hydrogen Storage Technologies—Key Challenges and Opportunities," *Materials Chemistry and Physics* 325 (2024): 129710, https://doi.org/10.1016/j.matchemphys.2024.129710.

7. J. Chen, S. Zhang, S. Chen, et al., "Theoretical Prediction of the Structural, Mechanical, Hydrogen Storage, Dynamic, Thermodynamic and Photoelectronic Properties of New Al-Based Hydrides X_2AlH_6 (X = K, Rb) for Hydrogen Storage Applications," *Journal of Physics and Chemistry of Solids* 210 (2026): 113345, https://doi.org/10.1016/j.jpcs.2025.113345.

8. F. Dawood, M. Anda, and G. M. Shafiullah, "Hydrogen Production for Energy: An Overview," *International Journal of Hydrogen Energy* 45 (2020): 3847–3869, https://doi.org/10.1016/j.ijhydene.2019.12.059.

9. T. Amirthan and M. S. A. Perera, "The Role of Storage Systems in Hydrogen Economy: A Review," *Journal of Natural Gas Science and Engineering* 108 (2022): 104843.

10. J. Ren, N. M. Musyoka, H. W. Langmi, M. Mathe, and S. Liao, "Current Research Trends and Perspectives on Materials-Based Hydrogen Storage Solutions: A Critical Review," *International Journal of Hydrogen Energy* 42 (2017): 289–311, https://doi.org/10.1016/j.ijhydene.2016.11.195.

11. Y. Kojima, "Hydrogen Storage Materials for Hydrogen and Energy Carriers," *International Journal of Hydrogen Energy* 44 (2019): 18179–18192, https://doi.org/10.1016/j.ijhydene.2019.05.119.

12. M. R. Usman, "Hydrogen Storage Methods: Review and Current Status," *Renewable and Sustainable Energy Reviews* 167 (2022): 112743, https://doi.org/10.1016/j.rser.2022.112743.

13. S.-Y. Lee, J.-H. Lee, Y.-H. Kim, et al., "Recent Progress Using Solid-State Materials for Hydrogen Storage: A Short Review," *Processes* 10 (2022): 304, https://doi.org/10.3390/PR10020304.

14. S. Niaz, T. Manzoor, and A. H. Pandith, "Hydrogen Storage: Materials, Methods and Perspectives," *Renewable and Sustainable Energy Reviews* 50 (2015): 457–469, https://doi.org/10.1016/j.rser.2015.05.011.

15. A. Züttel, "Hydrogen Storage Methods," *Die Naturwissenschaften* 91 (2004): 157–172.

16. A. S. Mekonnin, K. Wacławiak, M. Humayun, et al., "Hydrogen Storage Technology, and Its Challenges: A Review," *Catalysts* 15 (2025): 260, https://doi.org/10.3390/CATAL15030260.

17. H. Sun, Z. Wang, Q. Meng, and S. White, "Advancements in Hydrogen Storage Technologies: Enhancing Efficiency, Safety, and Economic Viability for Sustainable Energy Transition," *International Journal of Hydrogen Energy* 105 (2025): 10–22, https://doi.org/10.1016/j.ijhydene.2025.01.176.

18. E. Davies, A. Ehrmann, E. Schwenzfeier-Hellkamp, E. Davies, A. Ehrmann, and E. Schwenzfeier-Hellkamp, "Safety of Hydrogen Storage Technologies," *Processes* 12 (2024): 2182, https://doi.org/10.3390/PR12102182.

19. J. Li, X. Chai, Y. Gu, et al., "Small-Scale High-Pressure Hydrogen Storage Vessels: A Review," *Materials* 17 (2024): 721, https://doi.org/10.3390/MA17030721.

20. D. H. Kang, J. H. An, and C. J. Lee, "Numerical Modeling and Optimization of Thermal Insulation for Liquid Hydrogen Storage Tanks," *Energy* 291 (2024): 130143.

21. A. Naquash, N. Agarwal, M. Lee, A. Naquash, N. Agarwal, and M. Lee, "A Review on Liquid Hydrogen Storage: Current Status, Challenges and Future Directions," *Sustainability* 16 (2024): 8270, https://doi.org/10.3390/SU16188270.

22. S. S. A. Al Kareem, Q. Hassan, H. F. Fakhruldeen, et al., "A Review on Physical and Chemical Hydrogen Storage Methods for Sustainable Energy Applications," *Unconventional Resources* 8 (2025): 100235.

23. Z. Xie, Q. Jin, G. Su, et al., "A Review of Hydrogen Storage and Transportation: Progresses and Challenges," *Energies* 17 (2024): 4070, https://doi.org/10.3390/EN17164070.

24. K. Chen, M. Y. Lau, X. Luo, J. Huang, L. Ouyang, and X. S. Yang, "Research Progress in Solid-State Hydrogen Storage Alloys: A Review," *Journal of Materials Science & Technology* 246 (2026): 256–289, https://doi.org/10.1016/j.jmst.2025.05.037.

25. A. Salehabadi, M. F. Umar, A. Ahmad, M. I. Ahmad, N. Ismail, and M. Rafatullah, "Carbon-Based Nanocomposites in Solid-State Hydrogen Storage Technology: An Overview," *International Journal of Energy Research* 44 (2020): 11044–11058, https://doi.org/10.1002/er.5674.

26. Y. Li, Q. Guo, Z. Ding, et al., "MOFs-Based Materials for Solid-State Hydrogen Storage: Strategies and Perspectives," *Chemical Engineering Journal* 485 (2024): 149665, https://doi.org/10.1016/j.cej.2024.149665.

27. M. R. Kalibek, A. D. Ospanova, B. Suleimenova, et al., "Solid-State Hydrogen Storage Materials," *Discover Nano* 19 (2024): 195, https://doi.org/10.1186/s11671-024-04137-y.

28. Y. Xu, Y. Zhou, Y. Li, and Z. Ding, "Research Progress and Application Prospects of Solid-State Hydrogen Storage Technology," *Molecules* 29 (2024): 1767, https://doi.org/10.3390/MOLECULES29081767.

29. E. Nemukula, C. B. Mtshali, and F. Nemangwele, "Metal Hydrides for Sustainable Hydrogen Storage: A Review," *International Journal of Energy Research* 2025 (2025): 6300225, https://doi.org/10.1155/er/6300225.

30. A. Boretti, "A Narrative Review of Metal and Complex Hydride Hydrogen Storage," *Next Research* 2 (2025): 100226, https://doi.org/10.1016/j.nexres.2025.100226.

25130390, 2026, 9, Downloaded from https://advanced.onlinelibrary.wiley.com/doi/10.1002/adts.70534 by Turkey Cochrane Evidence Aid, Wiley Online Library on [31/08/2026]. See the Terms and Conditions (https://onlinelibrary.wiley.com/terms-and-conditions) on Wiley Online Library for rules of use; OA articles are governed by the applicable Creative Commons License

31. K. S. Nivedhitha, T. Beena, N. R. Banapurmath, et al., "Advances in Hydrogen Storage With Metal Hydrides: Mechanisms, Materials, and Challenges," *International Journal of Hydrogen Energy* 61 (2024): 1259–1273, https://doi.org/10.1016/j.ijhydene.2024.02.335.

32. N. D. Alkhaldi, "Study of Physical Characteristics and Hydrogen Energy Storage Capacity of Double Perovskite Hydrides X_2VH_6 (X = Li, Na, K) for Hydrogen Storage and Clean Energy Applications," *International Journal of Hydrogen Energy* 175 (2025): 151413, https://doi.org/10.1016/j.ijhydene.2025.151413.

33. H. Muhammad, A. Quader, H. B. Munir, M. Ahmed, A. Bakar, and H. E. Ali, "DFT Study of Structural, Electronic, Optical, Thermodynamic and Hydrogen Storage Properties of Be_2XH_6 (X = Co, Ni, Cu)," *International Journal of Hydrogen Energy* 180 (2025): 151703, https://doi.org/10.1016/j.ijhydene.2025.151703.

34. A. Candan, A. Erkisi, and B. Yildiz, "Revealing the Potential of Double Perovskite Hydrides A_2SiH_6 (A = Li and Na) for Solid-State Hydrogen Storage Applications," *Journal of Energy Storage* 132 (2025): 117957, https://doi.org/10.1016/j.est.2025.117957.

35. S. Zhang, S. Chen, Y. Chen, et al., "First Principles Study on the Structure, Hydrogen Storage, and Physical Properties of X_2VH_6 (X = Mg, Ca, Sr, Ba) Perovskite Hydrides for Hydrogen Storage Applications," *International Journal of Hydrogen Energy* 166 (2025): 150903, https://doi.org/10.1016/j.ijhydene.2025.150903.

36. G. Surucu, A. Gencer, A. Candan, H. H. Gullu, and M. Isik, "$CaXH_3$ (X = Mn, Fe, Co) Perovskite-Type Hydrides for Hydrogen Storage Applications," *International Journal of Energy Research* 44 (2020): 2345–2354, https://doi.org/10.1002/er.5062.

37. G. Surucu, A. Candan, A. Gencer, and M. Isik, "First-Principle Investigation for the Hydrogen Storage Properties of $NaXH_3$ (X= Mn, Fe, Co) Perovskite Type Hydrides," *International Journal of Hydrogen Energy* 44 (2019): 30218–30225, https://doi.org/10.1016/j.ijhydene.2019.09.201.

38. A. Gencer and G. Surucu, "Investigation of Structural, Electronic and Lattice Dynamical Properties of XNiH (X = Li, Na and K) Perovskite Type Hydrides and Their Hydrogen Storage Applications," *International Journal of Hydrogen Energy* 44 (2019): 15173–15182, https://doi.org/10.1016/j.ijhydene.2019.04.097.

39. M. Y. Akram and H. Dong, "First-Principles Study to Explore the Physical Properties of Perovskite Type Hydrides $XBaH_3$ (X = K and Rb) for Novel Hydrogen Storage System," *International Journal of Hydrogen Energy* 98 (2025): 211–218, https://doi.org/10.1016/j.ijhydene.2024.12.053.

40. T. Hashmi, M. Rizwan, M. A. Ullah, S. S. Ali, S. S. A. Gillani, and A. Ahmed, "Investigating Storage Capacity in Optically Active Perovskite Type Hydrides $XCaH_3$ (X: Na, Li and Cs) for Sustainable Hydrogen Storage Application," *Solid State Communications* 403 (2025): 116012, https://doi.org/10.1016/j.ssc.2025.116012.

41. A. Azdad, A. Boutahar, M. Balli, and H. Lemziouka, "First-Principles Study for the Hydrogen Storage Properties of $XCrH_3$ (X = Na, K, and Sr) Perovskite Type Hydrides," *Journal of Energy Storage* 141 (2026): 119194, https://doi.org/10.1016/j.est.2025.119194.

42. B. Ahmed, M. B. Tahir, A. Ali, and M. Sagir, "DFT Insights on Structural, Electronic, Optical and Mechanical Properties of Double Perovskites X_2FeH_6 (X = Ca and Sr) for Hydrogen-Storage Applications," *International Journal of Hydrogen Energy* 50 (2024): 316–323, https://doi.org/10.1016/j.ijhydene.2023.10.237.

43. A. Almahmoud, H. Alkhalidi, and A. Obeidat, "Comprehensive DFT Analysis of Structural, Mechanical, Electronic, Optical, and Hydrogen Storage Properties of Novel Perovskite-Type Hydrides Y_2CoH_6 (Y = Ca, Ba, Mg, Sr)," *Journal of Energy Storage* 117 (2025): 116146, https://doi.org/10.1016/j.est.2025.116146.

44. G. Kresse and J. Furthmüller, "Efficiency of Ab-Initio Total Energy Calculations for Metals and Semiconductors Using a Plane-Wave Basis Set," *Computational Materials Science* 6 (1996): 15–50, https://doi.org/10.1016/0927-0256(96)00008-0.

45. G. Kresse and J. Furthmüller, "Efficient Iterative Schemes for Ab Initio Total-Energy Calculations Using a Plane-Wave Basis Set," *Physical Review B* 54 (1996): 11169–11186, https://doi.org/10.1103/PhysRevB.54.11169.

46. J. P. Perdew, K. Burke, and M. Ernzerhof, "Generalized Gradient Approximation Made Simple," *Physical Review Letters* 77 (1996): 3865–3868, https://doi.org/10.1103/PhysRevLett.77.3865.

47. G. Kresse and D. Joubert, "From Ultrasoft Pseudopotentials to the Projector Augmented-Wave Method," *Physical Review B* 59 (1999): 1758–1775, https://doi.org/10.1103/PhysRevB.59.1758.

48. P. E. Blöchl, "Projector Augmented-Wave Method," *Physical Review B* 50 (1994): 17953.

49. J. D. Pack and H. J. Monkhorst, ""Special Points for Brillouin-Zone Integrations"—A Reply," *Physical Review B* 16 (1977): 1748–1749, https://doi.org/10.1103/PhysRevB.16.1748.

50. W. Tang, E. Sanville, and G. Henkelman, "A Grid-Based Bader Analysis Algorithm Without Lattice Bias," *Journal of Physics: Condensed Matter* 21 (2009): 084204.

51. R. F. W. Bader, *Atoms in Molecules* (Oxford Academic, 1990), https://doi.org/10.1093/OSO/9780198551683.001.0001.

52. A. M. Ganose, A. J. Jackson, and D. O. Scanlon, "SUMO: Command-Line Tools for Plotting and Analysis of Periodic Ab Initio Calculations," *Journal of Open Source Software* 3 (2018): 717, https://doi.org/10.21105/joss.00717.

53. Y. L. Page and P. Saxe, "Symmetry-General Least-Squares Extraction of Elastic Data for Strained Materials From Ab Initio Calculations of Stress," *Physical Review B* 65 (2002): 104104, https://doi.org/10.1103/PhysRevB.65.104104.

54. R. Hill, "The Elastic Behaviour of a Crystalline Aggregate," *Proceedings of the Physical Society Section A* 65 (1952): 349–354, https://doi.org/10.1088/0370-1298/65/5/307.

55. A. Togo, "First-Principles Phonon Calculations With Phonopy and Phono3py," *Journal of the Physical Society of Japan* 92 (2023): 012001, https://doi.org/10.7566/JPSJ.92.012001.

56. A. Togo, L. Chaput, T. Tadano, and I. Tanaka, "Implementation Strategies in Phonopy and phono3py," *Journal of Physics: Condensed Matter* 35 (2023): 353001.

57. K. Momma and F. Izumi, "VESTA 3 for Three-Dimensional Visualization of Crystal, Volumetric and Morphology Data," *Journal of Applied Crystallography* 44 (2011): 1272–1276, https://doi.org/10.1107/S0021889811038970.

58. D. J. Evans, "Computer 'Experiment" for Nonlinear Thermodynamics of Couette Flow," *The Journal of Chemical Physics* 78 (1983): 3297–3302, https://doi.org/10.1063/1.445195.

59. D. S. Lemons and A. Gythiel, "Paul Langevin's 1908 Paper "On the Theory of Brownian Motion" ["Sur la théorie du Mouvement Brownien," C. R. Acad. Sci. (Paris) 146 , 530–533 (1908)]," *American Journal of Physics* 65 (1997): 1079–1081, https://doi.org/10.1119/1.18725.

60. R. Jinnouchi, F. Karsai, and G. Kresse, "On-the-Fly Machine Learning Force Field Generation: Application to Melting Points," *Physical Review B* 100 (2019): 014105, https://doi.org/10.1103/PhysRevB.100.014105.

61. R. Jinnouchi, F. Karsai, C. Verdi, R. Asahi, and G. Kresse, "Descriptors Representing Two- and Three-Body Atomic Distributions and Their Effects on the Accuracy of Machine-Learned Inter-Atomic Potentials," *The Journal of Chemical Physics* 152 (2020): 234102, https://doi.org/10.1063/5.0009491/946337.

62. J. Behler and M. Parrinello, "Generalized Neural-Network Representation of High-Dimensional Potential-Energy Surfaces," *Physical Review Letters* 98 (2007): 146401, https://doi.org/10.1103/PhysRevLett.98.146401.

63. C. M. Bishop, *Pattern Recognition and Machine Learning* (Springer Nature, 2006).

64. M. E. A. El Goutni, S. Abdalla, M. Batouche, H. Ferjani, M. H. Dhaou, and A. Alsawi, "Design Principles for High-Performance Hydrogen Stor-

25130390, 2026, 9, Downloaded from https://advanced.onlinelibrary.wiley.com/doi/10.1002/adts.70534 by Turkey Cochrane Evidence Aid, Wiley Online Library on [31/08/2026]. See the Terms and Conditions (https://onlinelibrary.wiley.com/terms-and-conditions) on Wiley Online Library for rules of use; OA articles are governed by the applicable Creative Commons License

age in Li_2MH_6 (M = Si, Ge, Ti, Zn) Vacancy-Ordered Double Perovskites," *International Journal of Quantum Chemistry* 126 (2026): 70218.

65. M. E. A. El Goutni, H. Ferjani, M. Batouche, Y. G. Abou El-Reash, and T. Seddik, "Germanium-Based Double Perovskite Hydrides A_2GeH_6 (A = Li, Na, Be, Mg): A First-Principles Study for High-Capacity and Practical Hydrogen Storage," *Ceramics International* 52 (2026): 25085.

66. A. Mera and M. A. Rehman, "First-Principles Investigation for the Hydrogen Storage Properties of $AeSiH_3$ (Ae = Li, K, Na, Mg) Perovskite-Type Hydrides," *International Journal of Hydrogen Energy* 50 (2024): 1435–1447, https://doi.org/10.1016/j.ijhydene.2023.09.286.

67. "DOE Technical Targets for Onboard Hydrogen Storage for Light-Duty Vehicles | Department of Energy," can be found under https://www.energy.gov/eere/fuelcells/doe-technical-targets-onboard-hydrogen-storage-light-duty-vehicles.

68. L. X. Zhang, X. Y. He, X. H. Chen, S. F. Hasan, and T. Hussain, "Computational Evaluation of Scandium Decorated Boron Oxide Monolayer as Reversible Hydrogen Storage Medium," *International Journal of Hydrogen Energy* 197 (2026): 152597, https://doi.org/10.1016/j.ijhydene.2025.152597.

69. E. Darkaoui, J. Islah, K. Elasri, et al., "DFT and AIMD Investigation of New-Generation Vacancy Perovskites Hydrides A_2BeH_6 (A = Li, Na) for Hydrogen Storage Energy Application," *Journal of Physics and Chemistry of Solids* 217 (2026): 113805, https://doi.org/10.1016/j.jpcs.2026.113805.

70. Z. Abbas, A. Parveen, H. I. Elsaeedy, N. Mahjoub Said, and M. Taukeer Khan, "Revolutionizing Hydrogen Storage: A First-Principles Investigation of Hydrides Double Perovskites X_2SiH_6 (X = Mg, Ca, Sr) for Structural, Optoelectronic, and Mechanical Properties," *Materials Today Chemistry* 51 (2026): 103300, https://doi.org/10.1016/j.mtchem.2025.103300.

71. G. M. Mustafa, B. Younas, H. D. Alkhaldi, et al., "First Principle Study of Physical Aspects and Hydrogen Storage Capacity of Magnesium-Based Double Perovskite Hydrides Mg_2XH_6 (X = Cr, Mn)," *International Journal of Hydrogen Energy* 95 (2024): 300–308, https://doi.org/10.1016/j.ijhydene.2024.11.112.

72. X. Chen, L. Zhang, Z. Dai, et al., "Computational Investigation of Li-Decorated B14 as a Room Temperature Reversible Energy Storage Medium," *International Journal of Hydrogen Energy* 101 (2025): 1439–1447, https://doi.org/10.1016/j.ijhydene.2024.12.415.

73. J. Cheng, X. Chen, A. Hosen, J. Wang, M. R. Islam, and F. Zhai, "Na-Functionalized 2D a-C_5N_2 Monolayer as a Promising Candidate for Reversible Hydrogen Storage: Insights From First-Principles Calculations," *International Journal of Hydrogen Energy* 196 (2025): 152487, https://doi.org/10.1016/j.ijhydene.2025.152487.

74. X. Chen, J. Li, L. Zhang, et al., "Computational Evaluation of Li-Decorated $\alpha-$ C_3N_2 as a Room Temperature Reversible Hydrogen Storage Medium," *International Journal of Hydrogen Energy* 62 (2024): 510–519, https://doi.org/10.1016/j.ijhydene.2024.03.089.

75. L. Zhang, X. Chen, R. Zeng, et al., "Theoretical Investigation of Sodium Decorated B5N3 Boron Nitride Monolayer for Hydrogen Storage: A DFT Study," *Journal of Energy Storage* 152 (2026): 120822, https://doi.org/10.1016/j.est.2026.120822.

76. J. Wang, Y. Liu, Z. Dai, et al., "Evaluation of C18 as a Reversible Hydrogen Storage Material by First-Principles Calculations," *Journal of Energy Storage* 141 (2026): 119303, https://doi.org/10.1016/j.est.2025.119303.

77. Y. Selmani, A. Jabar, and L. Bahmad, "Insights Into the Physical Properties of Mg_2TiH_6 Hydride Double Perovskite for Solid-State Hydrogen Storage Applications: A First-Principles Calculations," *Journal of Energy Storage* 139 (2025): 118812, https://doi.org/10.1016/j.est.2025.118812.

78. P. Borlido, T. Aull, A. W. Huran, F. Tran, M. A. L. Marques, and S. Botti, "Large-Scale Benchmark of Exchange–Correlation Functionals for the Determination of Electronic Band Gaps of Solids," *Journal of Chemical Theory and Computation* 15 (2019): 5069–5079, https://doi.org/10.1021/acs.jctc.9b00322.

79. A. Gencer and G. Surucu, "Density Functional Theory (DFT) Study of BaScO3H0.5 Compound and Its Hydrogen Storage Properties," *Canadian Journal of Physics* 97 (2019): 1191, https://doi.org/10.1139/cjp-2018-0733.

80. M. Born, "On the Stability of Crystal Lattices. I," *Mathematical Proceedings of the Cambridge Philosophical Society* 36 (1940): 160–172, https://doi.org/10.1017/S0305004100017138.

81. F. Mouhat and F. X. Coudert, "Necessary and Sufficient Elastic Stability Conditions in Various Crystal Systems," *Physical Review B* 90 (2014): 224104, https://doi.org/10.1103/PhysRevB.90.224104.

82. A. Gencer, O. Surucu, G. Surucu, and E. Deligoz, "Anisotropic Mechanical Properties of $Tl_4AgI_8Te_{11}$ Compound With Low Thermal Conductivity," *Journal of Solid State Chemistry* 289 (2020): 121469, https://doi.org/10.1016/j.jssc.2020.121469.

83. S. F. Pugh, "XCII. Relations Between the Elastic Moduli and the Plastic Properties of Polycrystalline Pure Metals," *The London, Edinburgh, and Dublin Philosophical Magazine and Journal of Science* 45 (1954): 823–843, https://doi.org/10.1080/14786440808520496.

84. D. G. Pettifor, "Theoretical Predictions of Structure and Related Properties of Intermetallics," *Materials Science and Technology* 8 (1992): 345–349, https://doi.org/10.1179/mst.1992.8.4.345.

85. O. L. Anderson, "A Simplified Method for Calculating the Debye Temperature From Elastic Constants," *Journal of Physics and Chemistry of Solids* 24 (1963): 909–917, https://doi.org/10.1016/0022-3697(63)90067-2.

86. N. Miao, B. Sa, J. Zhou, and Z. Sun, "Theoretical Investigation on the Transition-Metal Borides With Ta_3B_4-Type Structure: A Class of Hard and Refractory Materials," *Computational Materials Science* 50 (2011): 1559–1566, https://doi.org/10.1016/j.commatsci.2010.12.015.

87. R. Gaillac, P. Pullumbi, and F. X. Coudert, "ELATE: An Open-Source Online Application for Analysis and Visualization of Elastic Tensors," *Journal of Physics: Condensed Matter* 28 (2016): 275201, https://doi.org/10.1088/0953-8984/28/27/275201.

Supporting Information

Additional supporting information can be found online in the Supporting Information section.

Supporting File: adts70534-sup-0001-SuppMat.docx.

25130390, 2026, 9, Downloaded from https://advanced.onlinelibrary.wiley.com/doi/10.1002/adts.70534 by Turkey Cochrane Evidence Aid, Wiley Online Library on [31/08/2026]. See the Terms and Conditions (https://onlinelibrary.wiley.com/terms-and-conditions) on Wiley Online Library for rules of use; OA articles are governed by the applicable Creative Commons License